Journal of Zhejiang University-SCIENCE A (Applied Physics & Engineering) in press
www.jzus.zju.edu.cn; www.springer.com/journal/11582
E-mail: jzus_a@zju.edu.cn

Research Article

https://doi.org/10.1631/jzus.A2500022

Flow field patterns in train compartments based on jet ventilation under variable air volume system: isothermal conditions

Songbo WU, Tian LI✉, Jiye ZHANG

State Key Laboratory of Rail Transit Vehicle System, Southwest Jiaotong University, Chengdu 610031, China

Abstract: Variable air volume systems are widely used in trains as they provide effective energy savings for air conditioning. However, the design phase is usually carried out at a certain fixed airflow, resulting in a difference between the expected and actual flow fields. In this study, we first analyzed the flow field characteristics at variable airflow rates under isothermal conditions, and subsequently established a correlation equation between the airflow and the flow field parameters. The results show that the airflow just entering the compartment conforms to the characteristics of an attached jet, then after converging in the middle, conforms to the characteristics of a free jet. The flow field characteristics are significantly correlated with the Reynold's number (*Re*) and are limited by the small space inside the vehicle. When the $Re \geq 2650$, the axial velocities all conform to the classical $u_m/u_0 \sim (x/b)^r$ or $u_m/u_0 \sim (y/b)^r$ law, the sectional velocities conform to the exponential and Gaussian distributions, and the characteristic thicknesses of the jets conform to a linear distribution. Derivation shows that the entrainment suction flow rate is related mainly to the initial flow rate and the air opening width. The results of study will inform the design of ventilation systems for high-speed trains.

Key words: high-speed train; internal flow field; ventilation; CFD simulation

Unedited

1 Introduction

With the development of urban construction and breakthroughs in key technologies, high-speed trains have become one of the most popular modes of transportation (Tian et al., 2019; Liu et al., 2024). The compartment of a high-speed train is an enclosed space, and passengers are often required to stay in the compartment for several hours. A good thermal comfort and cabin environment during train operation needs to be regulated by an efficient and reliable ventilation system (Li et al., 2019; Woodward et al., 2022; Wang et al., 2024b). How to create a healthy and comfortable cabin environment with low energy consumption is one of the key issues facing high-speed train designers. There are at least two challenges: the optimized design of the ventilation structure and the strategy applied under variable air volume air conditioning parameters.

Researchers have explored the ventilation systems of high-speed trains (Li et al., 2022; Schmeling et al., 2022; Liu et al., 2023; Yang et al., 2024). Lu et al. (2023) applied an improved proper orthogonal decomposition reconstruction method for multi-objective optimization of a high-speed train ventilation system, showing that ventilation parameter optimization significantly boosts air quality. Wang et al. (2024c) investigated reducing contaminant diffusion and infection risk in compartments by adjusting intake tract turbulence intensity, achieving an increase in decontamination rate from 0.23 to 1.86. Schmeling and Volkmann (2020) studied the interaction between ventilation methods and cabin thermal comfort, proposing a new low-momentum ventilation scheme. Wu et al. (2024) used experiments and numerical simulations to study formaldehyde distribution in high-speed train compartments, analyzing the link between ventilation parameters and concentration, revealing ventilation modes/parameters significantly influence its distribution. Chang et al. (2021) pro-

✉ Tian LI, litian2008@home.swjtu.edu.cn
Songbo WU, https://orcid.org/0000-0003-0153-0137
Tian LI, https://orcid.org/0000-0002-7345-7488

Received Jan. 21, 2025; Revision accepted June 3, 2025; Crosschecked

© Zhejiang University Press 2025

posed a novel hybrid ventilation system based on an original design, demonstrating improved thermal comfort and lower energy consumption. Aliahmadipour et al. (2017) explored summer train compartment flow field characteristics, noting improper design degrades the air environment, while structural improvements for symmetrical airflow enhance thermal comfort. Xu et al. (2022) investigated how different ventilation methods affect compartment flow fields and droplet diffusion, finding that top air supply reduces infection risk and inhibits virus longitudinal spread. Yang et al. (2018) studied the impact of different diffusers on thermal flow and pollutant distribution fields in compartments, showing that thermal plumes may cause pollutant locking. Scholars have also advanced variable air volume (VAV) ventilation strategies and design theories. Liu et al. (2011) analyzed dynamic cooling loads in train carriages during summer peak conditions, revealing significant regional and temporal variations. Wang et al. (2020) showed that VAV systems reduce energy consumption by 14.5% compared to fixed-volume systems, while inverter controls save 14.0-31.5% over on/off operation. Chen et al. (2024) developed an adaptive temperature control model considering air infiltration, thermal comfort, and energy consumption, achieving a 0.069 °C temperature error reduction and 1.534 kW-h energy savings per compartment. To address air-conditioning system time lag issues, Bai et al. (2008) proposed an adaptive PI controller with a Smith predictor, improving control stability. Zhang et al. (2015) introduced a model-free static pressure reset fuzzy control method for nonlinear VAV systems, achieving at least 7% energy savings. Relevant studies have also been conducted in the field of jet ventilation systems (Wang et al., 2024a). Han and Li (2021) investigated the velocity distribution of wall-attached jets in slotted-inlet ventilated spaces under isothermal conditions and derived unified mathematical equations to describe the decay of centerline velocity and the distribution of velocity profiles. Cao et al. (2010) conducted a series of experiments on ceiling-attached jets and their flow characteristics after impinging on a corner. They focused on the jet impingement region and the flow characteristics of the jet after deflection, proposing a virtual origin model for predicting the centerline velocity of the jet after deflection. Triboix and Marchal (2002) performed a stability analysis of the mechanism of jet attachment to walls and presented a formula relating the penetration distance and the height of the slot to the Archimedes number, based on the fundamental assumption of self-similar velocity and temperature profiles. Yu et al. (2003) carried out a scaled model study on the velocity and thermal fields of slotted ventilation ceilings under isothermal conditions, analyzing the airflow patterns, decay of centerline velocity and temperature, and velocity and temperature profiles, and established relevant semi-empirical predictive equations. Yin et al. (2021) studied the application and mechanism of air distribution of column-attached ventilation in winter heating conditions and found that the *Ar* (Archimedes number) is related to air distribution and ventilation effectiveness. An *Ar* value less than 2.241×10^{-3} is a prerequisite for effective airflow, and the heat transfer efficiency is negatively and linearly correlated with the *Ar* value.

The above research shows that VAV systems can effectively save energy. However, most of these studies have concentrated on ventilation system design under fixed air volume conditions. This focus has left a gap in addressing the dynamic challenges encountered during train operation, such as fluctuations in heat load and external climate conditions. These dynamic factors can lead to mismatches between the fixed air volume design and actual requirements, resulting in either excessive or insufficient cooling/heating capacity. This not only causes unnecessary energy consumption but also compromises passenger thermal comfort. Moreover, current VAV control strategies are largely based on preset static parameters, which severely limit their ability to adapt to the real-time variations in the in-car flow field heat load. To bridge this gap, in the present study we endeavored to uncover the evolution patterns of the flow field under both isothermal and variable air volume conditions. By establishing correlation equations between air volume and flow field parameters, we aimed to provide a robust theoretical foundation for the development of intelligent ventilation control systems. This advancement is expected to offer innovative solutions for enhancing thermal comfort while simultaneously achieving energy savings. The findings of this study are expected to hold substantial reference value for the evolution of ventilation systems within the rail transit industry, potentially

Unedited

guiding future advancements towards more efficient and adaptive designs.

2 Turbulence Model

The air flow in train compartments is a low-speed turbulent flow, and the flow field information can be predicted by solving the incompressible Navier-Stokes equations. Realizable k-ε is a classical two-equation model shown to be sufficiently accurate in predicting the flow field in compartments (Wu et al., 2023; Cao et al., 2022;). Therefore, this model was used here for flow field prediction with an enhanced wall function for the near-wall surface. The generalized governing equations were as follows:

$$\frac{\partial}{\partial t}(\rho k)+\frac{\partial}{\partial x_j}(\rho k u_j)=\frac{\partial}{\partial x_j}\left[\left(\mu+\frac{\mu_t}{\sigma_k}\right)\frac{\partial k}{\partial x_j}\right] + G_k+G_b-\rho\varepsilon-Y_M+S_k, \tag{1}$$

$$\frac{\partial}{\partial t}(\rho \varepsilon)+\frac{\partial}{\partial x_j}(\rho \varepsilon u_j)=\frac{\partial}{\partial x_j}\left[\left(\mu+\frac{\mu_t}{\sigma_\varepsilon}\right)\frac{\partial \varepsilon}{\partial x_j}\right] + \rho C_1 S\varepsilon-\rho C_2\frac{\varepsilon^2}{k+\sqrt{\nu\varepsilon}} + C_{1\varepsilon}\frac{\varepsilon}{k}C_{3\varepsilon}G_b+S_\varepsilon, \tag{2}$$

$$C_1=\max\left[0.43,\frac{\eta}{\eta+5}\right],\eta=S\frac{k}{\varepsilon},S=\sqrt{2S_{ij}S_{ij}}, \tag{3}$$

where, t is the physic time; ρ is the air density; u_j is the air velocity; G_b and G_k are the generation of turbulent kinetic energy due to buoyancy and the mean velocity gradients, respectively; Y_M represents the contribution of fluctuating dilatation incompressible turbulence to the overall dissipation rate; k and ε are the turbulent kinetic energy and turbulent dissipation rate, respectively; σ_k and σ_ε are the turbulent Prandtl number for k and ε, respectively; C_2 and $C_{1\varepsilon}$ are constants; and S_k and S_ε are user-defined source terms.

3 Computational Model

3.1 Numerical model

A full-size geometric model was developed based on the carriages of a high-speed train that is in service. The length, width and height of the carriages are about 18300 mm, 3200 mm and 2300 mm respectively. The occupants of a car in fully loaded condition total 90, with a 3+2 seating distribution. The air intake of the cabin is located on both sides of the ceiling and the exhaust is located on both sides of the floor (Fig. 1).

Table 1: Cases for the isothermal jet (b=20 mm)

	Q (L/(s·person))	ΔT (°C)	u_0 (m/s)	Re
Case.1	6	0	0.735	990
Case.2	8	0	0.980	1330
Case.3	10	0	1.225	1660
Case.4	12	0	1.470	1990
Case.5	14	0	1.714	2320
Case.6	16	0	1.960	2650
Case.7	18	0	2.204	2980
Case.8	20	0	2.449	3310

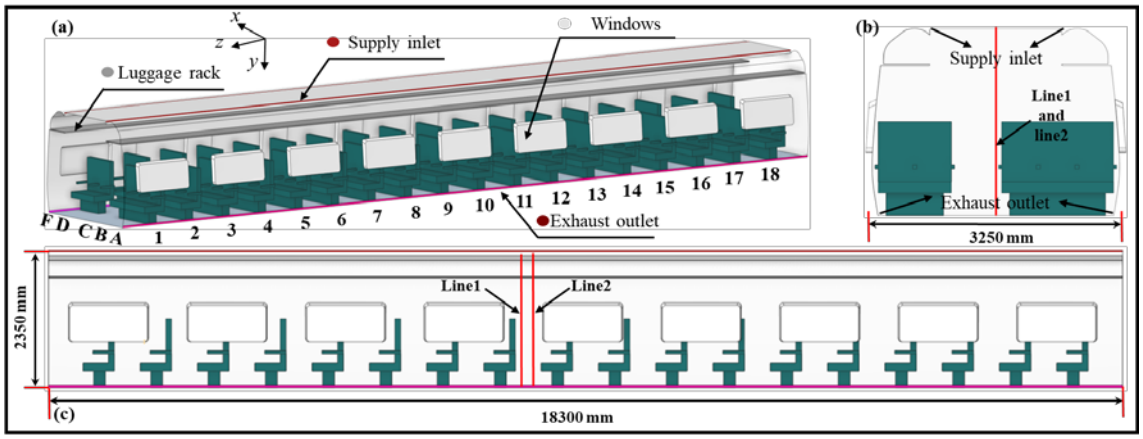

Fig. 1. Geometric model of the train carriage.

The cases for the isothermal jet are given in Table 1. When calculating the Reynolds number (Re), the characteristic length is taken as the slit width of the air supply opening, which is specifically b = 20 mm. To reveal the effect of different Re numbers on the jet law, several sets of small and large airflow

Unedited

conditions were also selected. Here, the calculated working conditions included 6 L/(s·person) ~ 20 L/(s·person), corresponding to *Re* numbers of 993~3311, respectively.

3.2 Boundary conditions

The carriages of high-speed trains are relatively closed, and the indoor environment is uniformly regulated by the air-conditioning system. The airflow in the compartment is small and incompressible, and its material properties are considered to be incompressible ideal gases. Here, we assumed that the air flow was fully mixed and uniformly distributed before entering the passenger compartment. Therefore, the boundary condition of the air supply outlet was set as a velocity-inlet, and the magnitude of the velocity was a fixed value (Lu et al., 2023). The air supply temperature of the air conditioner was set at 22°C, and the flow rate was determined by the specific calculation conditions. Since the distribution of the specific flow parameters at the air exhaust outlet is complex and difficult to determine, the boundary condition was set as an outflow. This method can automatically adjust the state at the outlet according to the internal flow situation. During the operation of the train, the flow field inside the car will be affected by the solar thermal radiation and the heat conduction of the car body. Here, we assumed that the ambient temperature was 35 °C and the solar radiation intensity 800 W/m² (Li et al., 2022; Xu et al., 2022). Considering the differences in structural design, material properties, and processing techniques, the heat transfer coefficients of the side walls, floor, end walls, and windows were set to 0.9, 1.2, 1.2, and 1.4 W/(m^2·K), respectively (Wu et al., 2023).

In the solution of the Navier-Stokes equations, the realizable *k*-*ε* turbulence model was selected, and enhanced wall functions were used to handle the near-wall region. The SIMPLE (Semi-Implicit Method for Pressure-Linked Equations) algorithm was chosen to solve the pressure-velocity coupling terms. The Least Squares Cell Based method was selected for calculating the physical quantity gradients on the grid cells. The PRESTO! (Pressure Staggering Option) discretization scheme was adopted for pressure, and second order upwind discretization schemes were used for turbulent kinetic energy, turbulent dissipation rate, momentum, and energy.

3.3 Mesh Independence

To ensure that the computational results were not affected by the numerical grids, grid independence verification was first needed. The numerical grid division of the carriage model was carried out using Fluent Meshing software, with the Poly grid type. Three sets of grids with different scales were divided, and the number of body grids was about 6.8, 21.7 and 34.5 million, respectively. The maximum size of the body grid corresponded to 36, 28 and 20 mm, respectively. To ensure that *y+* was less than 3 in most regions, a 2-layer boundary layer was delineated, with the height of the first boundary layer being 2 mm. Figure 2 illustrates the computational results of 3 sets of grids, including velocity and temperature values on 2 sampling lines, with the exact locations of the sampling lines shown in Fig. 1. Calculation results showed that the change rule of each physical quantity was consistent showed a small deviation when using medium or fine grids. Considering the calculation accuracy and calculation speed, the medium grid was used here for calculation. The specific dimensions were: the surface grid size of the air supply and exhaust vents were 2 mm and 5 mm, respectively; the surface grid size of the seats and the train was 24 mm; and the maximum size of the body grid was 28 mm. Figure 3 shows a schematic diagram of the grid. Details of the verification of numerical methods are given in Section S1 of the supplementary file.

4 Results

First, we analyzed the interrelationship between variable air volume ventilation and flow field characteristics under isothermal conditions. Subsequently, we established the correlation equation for the interaction between the variable air volume and the flow field parameters in the vehicle by combining Prandtl turbulence hypothesis and some classical theories.

Unedited

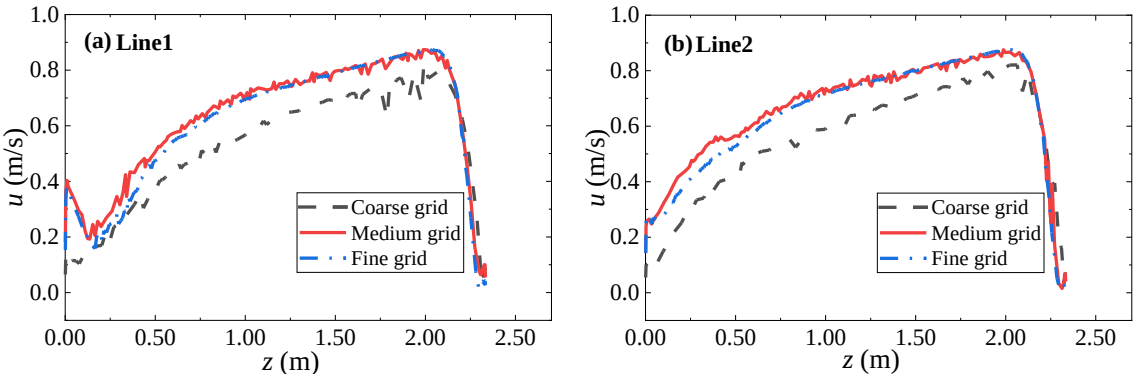

Fig. 2. Grid independence test: (a) line1, and (b) line2.

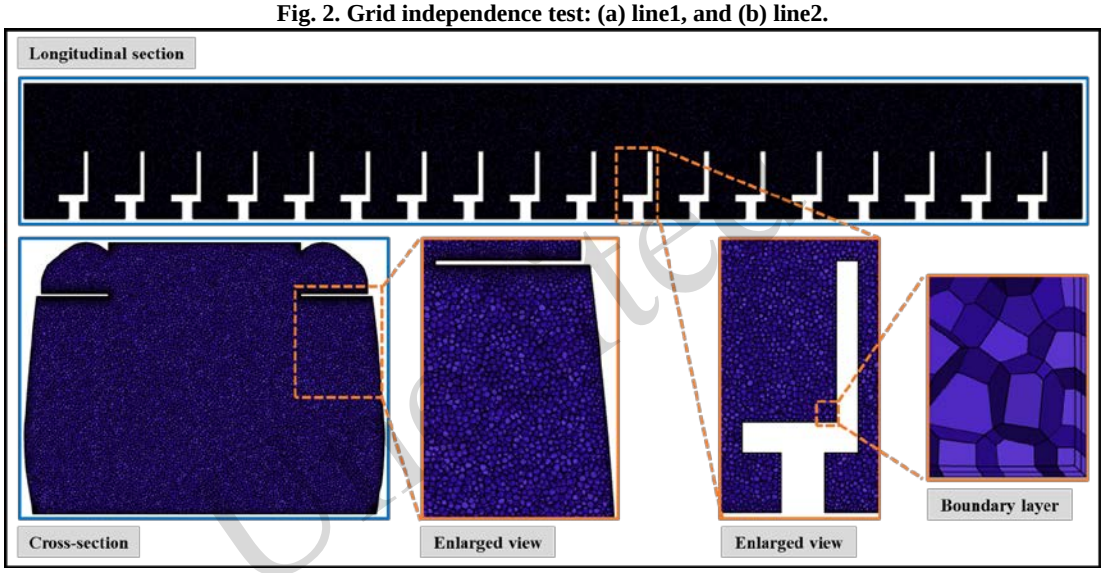

Fig. 3. Mesh generation.

4.1 Air flow characteristics

4.1.1 Distribution of velocity field

Figure 4 illustrates the velocity field distribution under different *Re* values. When the jet flow enters the compartment, it immediately adheres to the ceiling surface due to the Coanda effect, a phenomenon where fluid flow tends to attach to a nearby surface, presenting characteristics typical of an adherent jet. After converging at the mid-ceiling position, the airflow begins to diffuse downward, exhibiting features of a free jet. In this free jet stage, the airflow is no longer restricted by surface attachment, enabling unrestricted spreading. Driven by the two jet flow volumes, part of the airflow forms a large-scale airflow circulation in the passenger area. The velocity field distribution is significantly influenced by the *Re* (Fig. 4). Quantitatively, there is a positive correlation between the overall airflow velocity in the vehicle and the *Re*, meaning the airflow velocity increases as the *Re* number rises. Notably, across all six *Re* values investigated, a fixed pattern of fully circulating airflow is generated in the compartment. Although the velocity field allows for qualitative analysis of the flow field (e.g., observing flow patterns and circulation structures), quantitative analysis remains essential. This is because quantitative methods can reveal intrinsic properties of the compartment's flow field, such as precise velocity magnitude distributions, circulation intensity metrics, and dynamic flow characteristics that cannot be fully captured through qualitative observation alone.

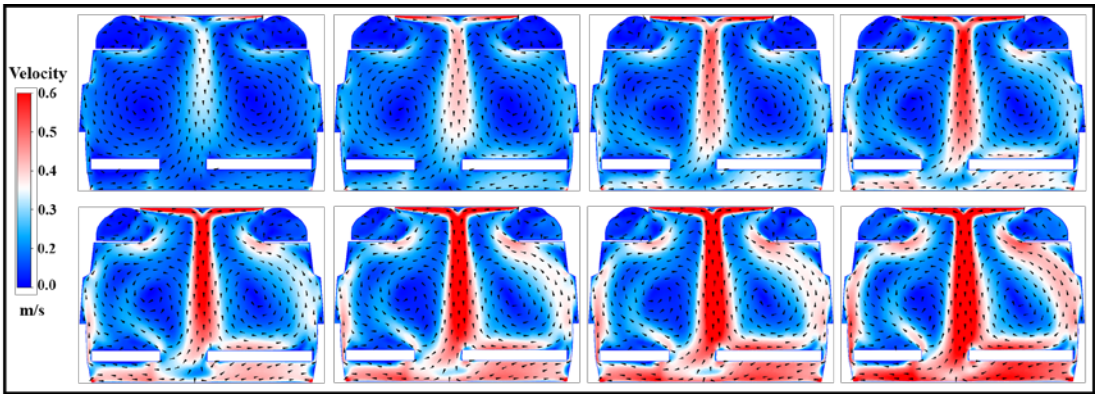

Fig. 4. Time-averaged velocity vector fields at different Reynolds numbers.

Note that two right-angle coordinate systems are involved in the flow field analysis, *x*—*y* and *x**—*y*, with the *z*-axis perpendicular to the cross-section. The coordinate origin is located at the outlet of the air supply when analyzing the attached jet (Fig. 5a) and in the middle of the top of the compartment when analyzing the free jet (Fig. 5b). Four monitoring lines were established along the *x*-direction and six in the *y*-direction to monitor the velocity profile of the flow field in the compartment (Fig. 5). The four positions along the *x*-direction were 150, 300, 450 and 600 mm. The six positions along the *y*-direction were 300, 600, 900, 1200, 1500 and 1800 mm.

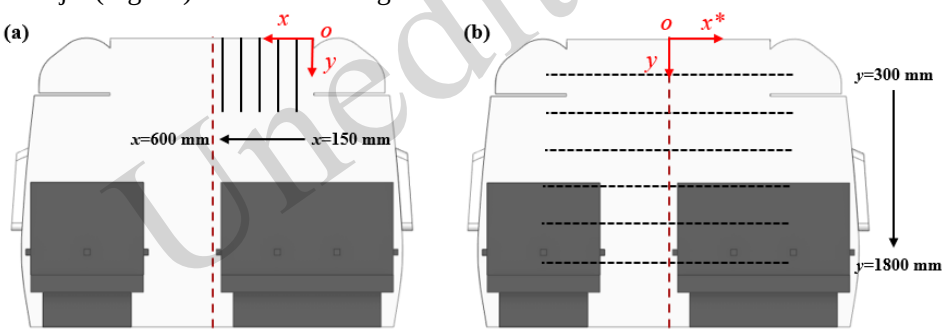

Fig. 5. Schematic diagram of the location of the monitoring lines in the compartment.

Figure 6 illustrates the velocity profiles at four positions along the *x*-direction. For comparison, the velocity profiles are dimensionless using the axial velocity (u_m) of the location, and the dimensionless parameter is u/u_m. The location of the maximum axial velocity at the same position for different *Re* numbers is essentially certain. After the jets are ejected from the slit, they all show the characteristics of attached jets. In the inner layers of the attached jets, the dimensionless velocity profiles essentially overlap, exhibiting Reynolds-independence. In the outer layer of the attached jet, the jet thickness decreases as the *Re* increases, and the dimensionless velocity (u/u_m) at the same location is smaller. Below the main region of the jet, the dimensionless velocities at low *Re* numbers ($Re \leq 1330$) are larger and more capable of inducing cyclonic rise in the flow. It may be that the dominant vortex structure within the shear layer at low *Re* numbers is larger, and its relative entrainment and sucking capacity is stronger and more capable of promoting the development of the jet. This is in general agreement with the findings of Suresh (2008) and Cao (2014). As the distance from the jet outlet position increases, the thickness of the jet also gradually increases, and the ability to coil and suck the airflow gradually increases. However, this difference decreases with increasing *Re* numbers, and the velocity profiles at high *Re* numbers ($Re \geq 2320$) gradually show Reynolds-independence.

Unedited

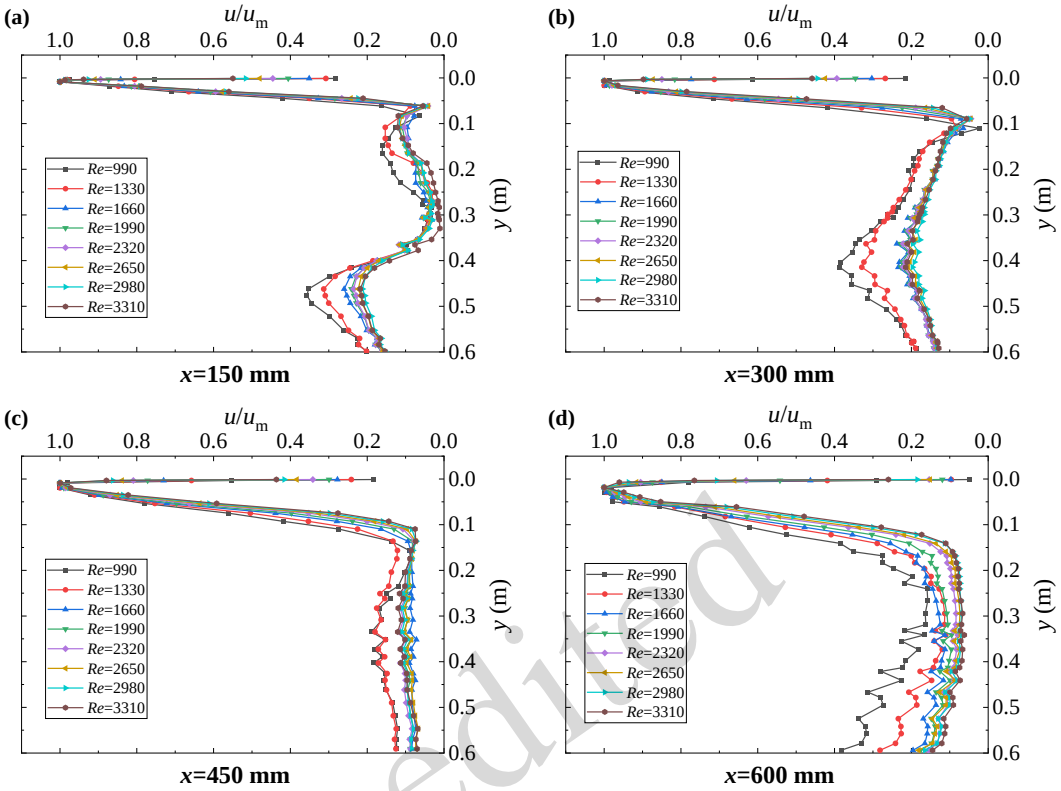

Fig. 6. Cross-sectional velocity distribution in the attached jet region: (a) x=150 mm; (b) x=300 mm; (c) x=450 mm; (d) x=600 mm.

Unedited

Fig. 7 illustrates the dimensionless velocity profiles at the six positions along the y-direction. Similarly, the locations of the maximum axial velocities at different Re numbers are essentially the same and are located in the mid-section region of the compartment (x = 0 m). The velocity development pattern in the middle of the compartment exhibits some free jet characteristics, but its development pattern can be equally limited by the space of the compartment. Two sets of vortex structures are formed on both sides of the free jet under the dual effect of jet entrainment and compartment micro space. As the jet progresses downward, the thickness of the jet gradually increases. In contrast, the region outside the main jet is significantly affected by the vortex structure. At the same location, the thickness and dimensionless velocity of the jet at low Re numbers ($Re \leq 1330$) are larger, which suggests that it is more efficient in entrainment of the surrounding air. As the Re number increases, the thickness of the jet gradually increases, but the rate of change of the increase decreases, and the velocity profiles at high Re numbers largely overlap. Note that when y = 1800 mm, the velocity profile law is affected differently by the asymmetric seat.

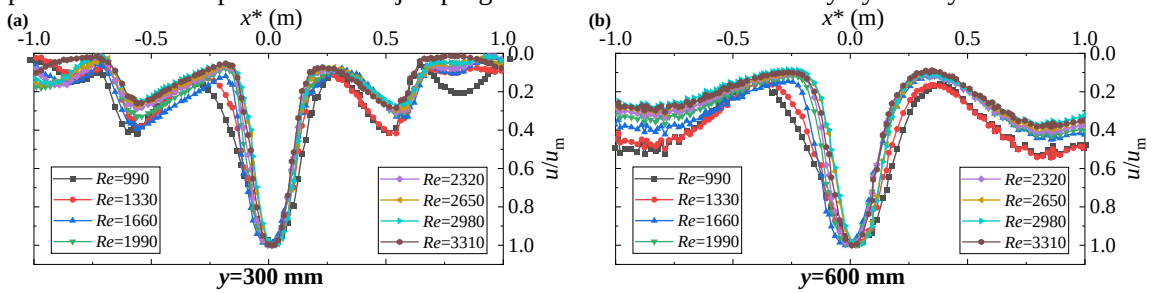

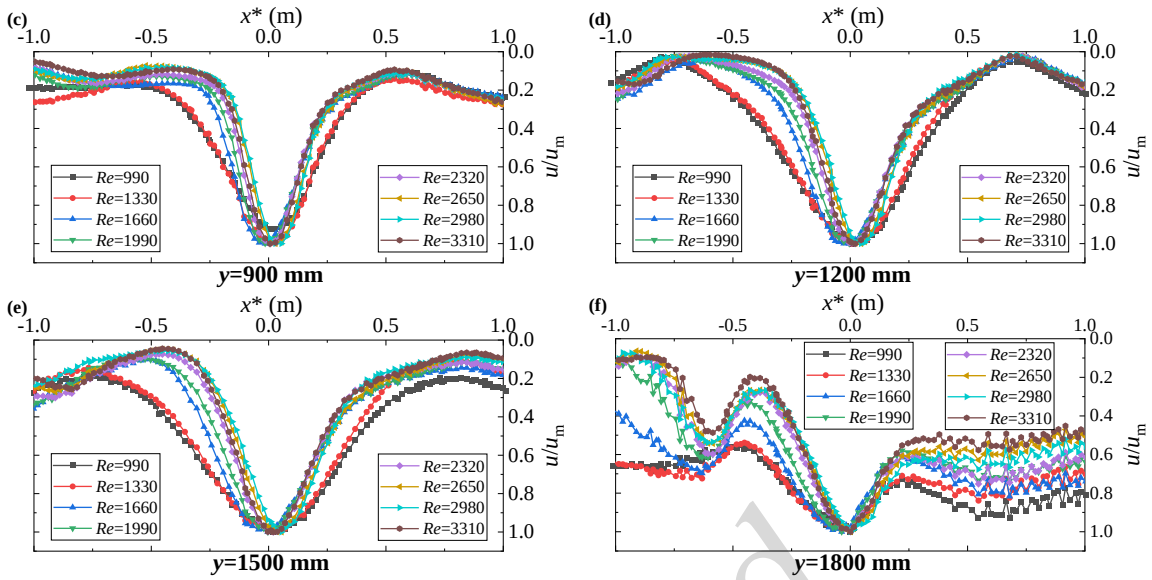

Fig. 7. Cross-sectional velocity distribution in the free jet region: (a) *y*=300 mm; (b) *y* =600 mm; (c) *y* =900 mm; (d) *y* =1200 mm; (e) *y* =1500 mm; (f) *y* =1800 mm.

4.1.2 Distribution of vorticity field

As the jet develops, it constantly entrains and sucks in the surrounding gases and creates a vortex structure. These vortex structures play an important role in the development of the jet and the distribution of the flow field. Figure 8 shows the time-averaged vorticity field distribution at different *Re* numbers. The positivity and negativity of the vorticity field gives a clear picture of the rotational direction of the flow as well as the shear and boundary layers of the attached jet. For the attached and free jet regions, the line of intersection between the two is the center axis of the jet. For adherent jets, the centerline gradually bends downward. For free jets, the centerline is essentially located in the middle of the compartment. As the *Re* number increases, the strength of the vortex structure gradually increases. This indicates that the jet entrainment capacity is also increasing and is capable of suctioning more surrounding air, which is conducive to improving the ventilation efficiency of the system.

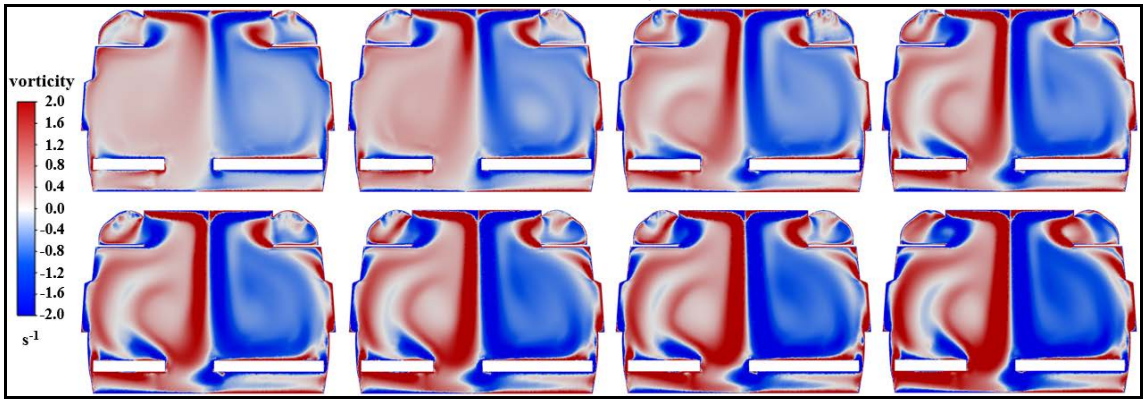

Fig. 8. Time-averaged vortex fields at different Reynolds numbers.

The main drivers behind the continuous development and expansion of the jet are the guidance and entrainment of the external airflow via the entrainment effect, which in turn gives rise to a vortex structure. To analyze the similarity in vorticity across different *Re* numbers and nullify the impact of units, we rendered the vorticity dimensionless. Its definition was as follows:

$$w' = w \times \frac{b}{u_0} = \left(\frac{\partial u_z}{\partial y} - \frac{\partial u_y}{\partial z}\right)\frac{b}{u_0}, \tag{4}$$

Unedited

where w represents the vorticity; w' represents the dimensionless spanwise vorticity; and u_y and u_z denote the velocity scalars of the airflow in the y-direction and z-direction, respectively.

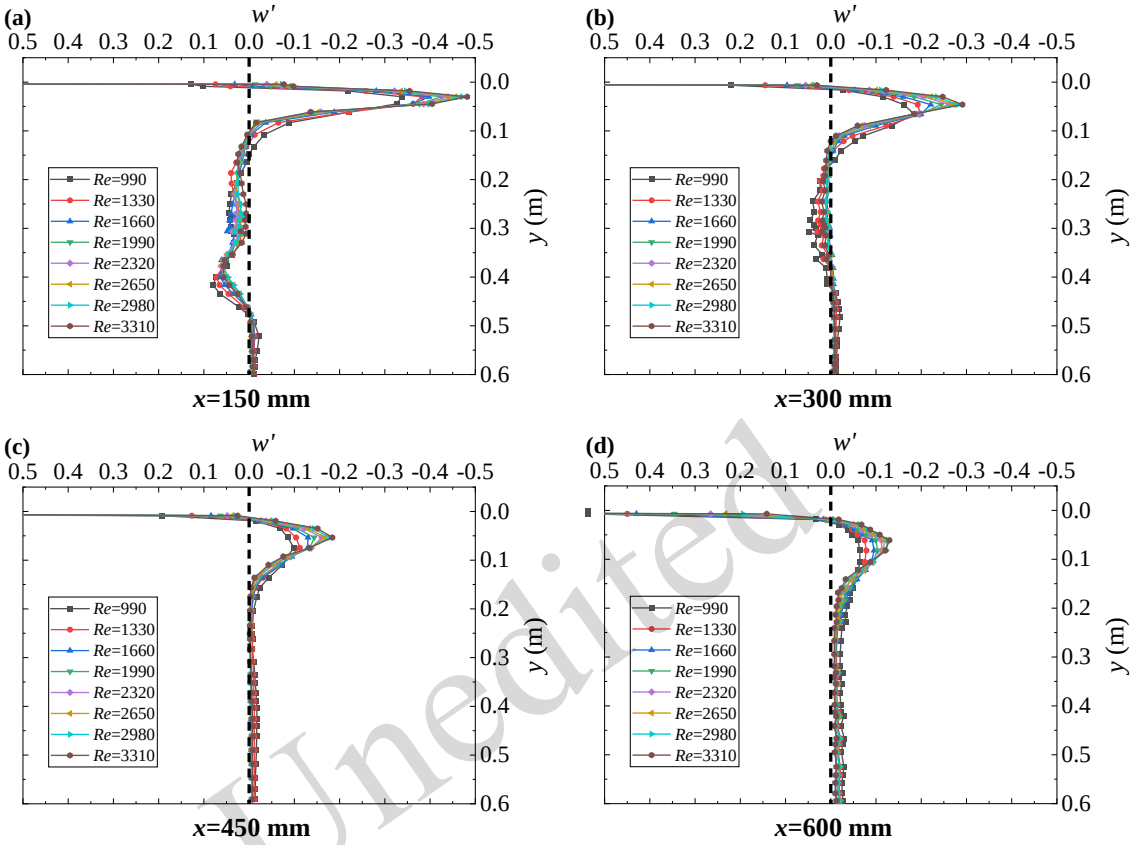

Fig. 9 Dimensionless vorticity profiles in the region of the attached jet: (a) x=150 mm; (b) x=300 mm; (c) x=450 mm; (d) x=600 mm.

Fig. 9 illustrates the dimensionless vorticity distribution within the attached jet region. When $Re \geq 990$, a consistent pattern emerges in the vorticity distribution. Near the wall boundary layer, the vorticity is positive and relatively high, but it swiftly diminishes to zero. This transition point marks the interface between the boundary layer and the shear layer, and this change occurs very abruptly. Following this, the vorticity surges sharply in the positive direction, reaching a peak value before gradually subsiding. Overall, the vorticity is notably higher in the inner jet region, which signifies a stronger vortex structure and enhanced entrainment capability. Conversely, in the outer jet region, the vorticity is relatively low and continues to decrease with increasing distance (y). When $x \geq 300$ mm and the jet has fully developed into the main flow region, the vorticity approaches zero. Additionally, as the entrainment flow increases and the jet momentum diminishes, the vorticity also progressively decreases with increasing distance x. This trend indicates that both the strength of the vortex structure and the entrainment ability of the jet weaken as the jet develops from the inner to the outer regions and from the near to the far field. Moreover, the dimensionless vorticity increases with a higher Re number, suggesting improved entrainment efficiency per unit flow. However, note that the gradient of this increase diminishes with rising Re values and eventually becomes independent of the Re number.

4.2 “Parameter- flow field” theoretical calculation

From the flow field analysis, the air flow entering the carriage undergoes two stages successively: attached jet flow (Region I) and free jet flow (Region II). Details are given in Section S2 of the supplementary file. In this section we describe the “parameter-field” theoretical calculation for the attached and free jet regions under isothermal conditions, including the axial velocity distribution law, the

Unedited

section velocity distribution law, the characteristic thickness of the jet, and the jet entrainment volume.

4.2.1 Distribution of jet axial velocity

Based on extensive experimental observations, in the longitudinal expansion of turbulent jets, both the longitudinal time-averaged velocity and axial velocity gradually decay. Due to the similarity of the time-averaged velocity in the main body section of the jet, combined with the coordinate system in Fig. 5, the axial velocity distribution in the attached jet region can be set as $f(u_m/u_0, x/b)=0$, and in the free jet region as $f(u_m/u_0, y/b) = 0$.

Relevant studies have derived the distribution law of jet axial velocity. Details are given in Section S3 of the supplementary file. The derivation of the above equations is based on multiple assumptions and experimental parameters from simplified models, such as Prandtl's new turbulence hypothesis and the similarity of turbulent shear stress. However, jet ventilation in train carriages is constrained by more complex geometric spaces and air outlet types. Therefore, certain discrepancies exist, and based on the derivation, it can be assumed that:

$$\frac{u_0}{u_m} \sim \left(\frac{x}{b_{slot}}\right)^r, r>0, \tag{5}$$

where, r can be determined by experiments and reflects the momentum decay rate of the jet.

The law of variation of dimensionless velocity (u_m/u_0) along the axis is given in Fig. 10. Figure 10a shows the axial velocity in the region of the attached jet and Fig. 10b the axial velocity in the region of the free jet. Theoretical calculations of incompressible flows for turbulent boundary layers have not developed enough to allow a move away from semi-empirical theories. Here, we attempt to establish a semi-empirical formula for the axial velocity of train ventilation in conjunction with the theoretical analysis of the Prandtl turbulence hypothesis. In the region of attached jets, the decay rate of dimensionless axial velocities increases with decreasing *Re* number. As a result, the axial velocities at low *Re* numbers are relatively small in the trailing region of the free jet, which also leads to relatively small initial velocities in the free jet region. When $Re \geq 2650$, the decay rates of the attached jets are basically the same. Therefore, for jets with $Re \geq 2650$, the decay law of the jet axial velocity before reaching the collision zone ($x/b \leq 32.5$) can be described uniformly as:

$$\frac{u_m}{u_0} = \frac{1}{0.007\left(\frac{x}{b}\right)^{1.46}+1}, \tag{6}$$

In the free jet region, the jet decay rate is essentially the same, with the jet decaying relatively slowly. When y/b = 15, at u_m/u_0 between 0.35 and 0.45, and when y/b = 95, at u_m/u_0 near 0.25, after fitting, it is found that for jets with $Re \geq 2650$, the decay law of the jet axial velocity in the free jet range ($15 \leq y/b \leq 95$) can be described uniformly as:

$$\frac{u_m}{u_0} = \frac{0.446}{3.37\times10^{-8}\left(\frac{y}{b}\right)^{3.7}+1}, \tag{7}$$

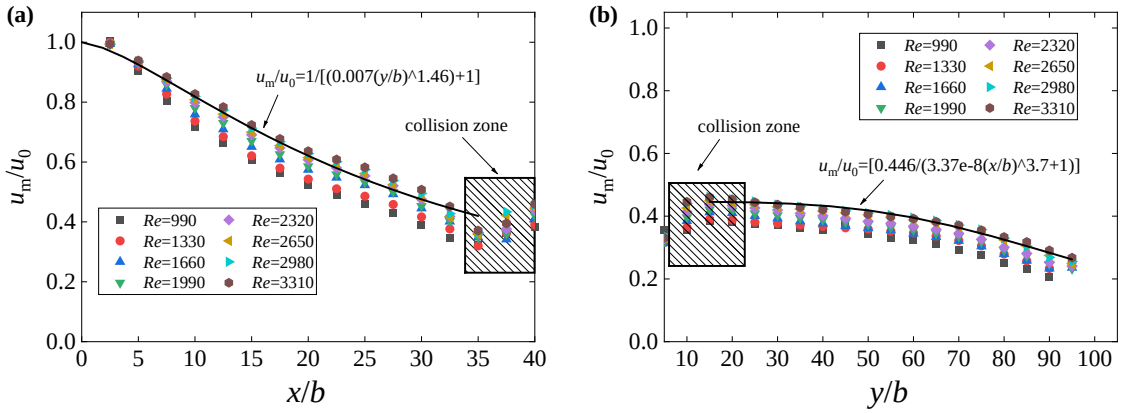

Fig. 10 Jet axial velocity distribution at different Reynolds numbers: (a) attached jet region; (b) free jet region.

4.2.2 Distribution of section velocity

For an attached jet air supply, according to the classical theoretical studies of Glauert (1956), Schwarz and Cosart (1961), and Verhoff (1963), the velocities within the jet zone conform to an exponential form of distribution and show similarity in the

Unedited

velocities at different cross-sections. The theoretical velocity profile in the laminar state is given by the Glauert tabulation. The theoretical velocity profiles in the turbulent state are given by the Schwarz and Cosart (1961) and Verhoff (1963) theories, respectively, as follows:

$$\frac{u}{u_m} = \exp[-0.973(y/\delta_{0.5}-0.14)^2], \quad (8)$$

$$\frac{u}{u_m} = 1.48(y/\delta_{0.5})^{1/7}[1-\mathrm{erf}(0.68y/\delta_{0.5})], \quad (9)$$

where exp is the exponential function and erf is the error function.

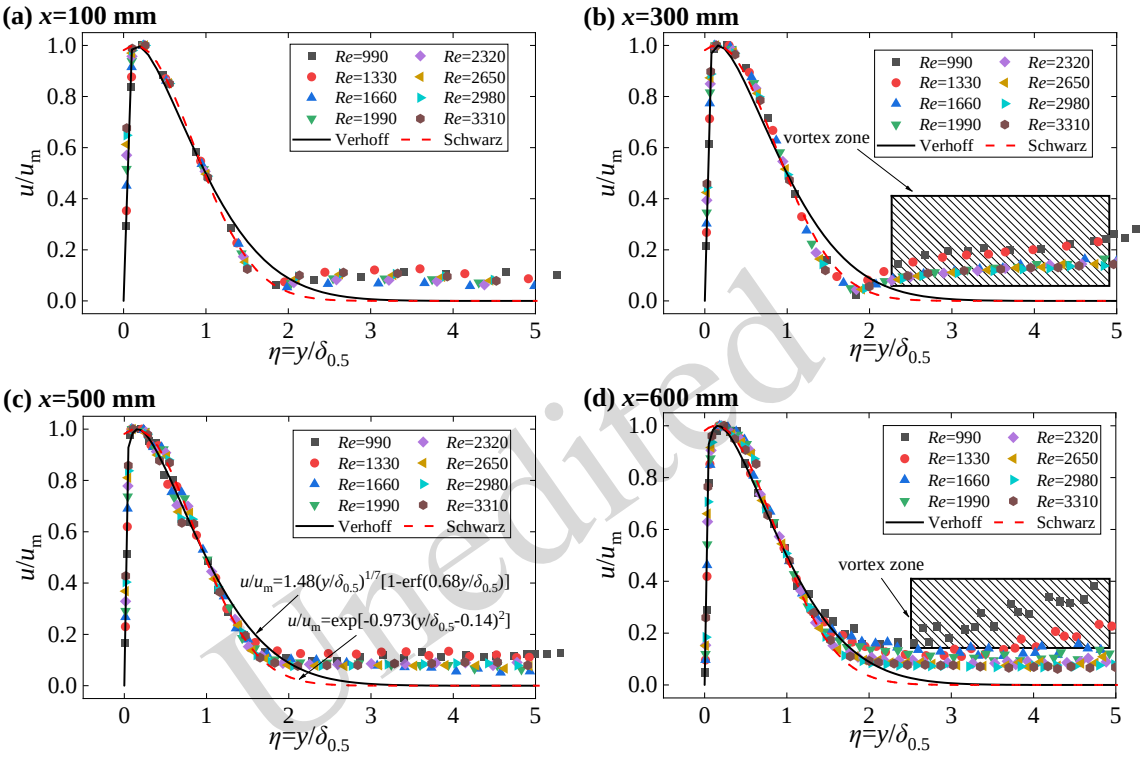

Fig. 11. Section velocity distribution of an attached jet at different Reynolds numbers: (a) *x*=100 mm; (b) *x*=300 mm; (c) *x*=500 mm; (d) *x*=600 mm.

Four jet profiles were selected for comparative analysis: for x=100 mm, x=300 mm, x=500 mm and x=600 mm. Figure 11 shows that within the main jet zone ($0 \le \eta \le 2$), the section velocities are in good agreement with the classical theory. Within the near-wall zone, the velocity increases rapidly from the wall and reaches a maximum value at about η = 0.25. In the interval $0.25 \le \eta \le 2$, the section velocity begins to decrease gradually until the outer edge of the jet converges with the ambient velocity. Outside the main jet region ($\eta > 2$), the velocity is gradually influenced by the surrounding flow field. When $Re \ge$ 1660, the flow field outside the main flow zone also has high similarity. When the vortex structure exists outside the mainstream region, the velocity distribution is significantly affected by the vortex.

From experimental study and theoretical analysis, it shows that free turbulent jets are characterized by the similarity of the velocity distribution in the cross-section and linear expansion of the jet boundary (Liu, 2008). In addition, during the jet flow, the velocity distribution of the jet section is characterized by a Gaussian distribution due to vortex pairing and entrainment. Solved according to the classical theory of Tollmien, the section velocity solution for a free jet can be described by (Liu, 2008):

$$\frac{u}{u_m} = \left(0.86 + \frac{0.14}{1+\left|\frac{x^*}{\delta_{0.5}}\right|}\right)\exp[-0.621(x^*/\delta_{0.5})^2], \quad (10)$$

Two jet profiles were selected for comparative analysis, taken from a height of 1700 mm (y=600 mm) and 1100 mm (y=1200 mm) from the floor. Figure 12 shows that the velocity distribution is consistent with the Gaussian distribution in the main jet region ($-2 \le \eta$

Unedited

≤ 2). Considering that the jet axis may be shifted, its center is not necessarily at x=0 mm. Especially at y=1200 mm, it may be affected mainly by the distribution of seats.

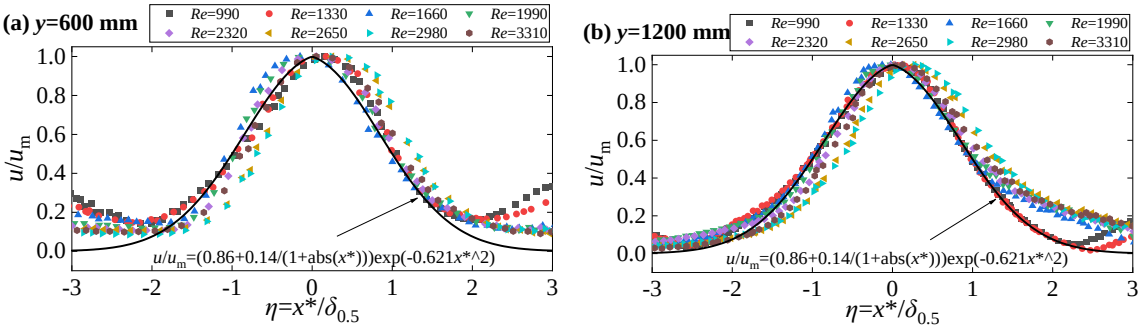

Fig. 12. Section velocity distribution of a free jet at different Reynolds numbers: (a) y=600 mm; (b) y=1200 mm.

4.2.3 Jet characteristic thickness

As mentioned above, the jet characteristic thickness (jet boundary) increases linearly. According to our data fitting, the characteristic thickness of the jet at different *Re* numbers also conforms to the law of linear growth, which is consistent with the theoretical derivation.

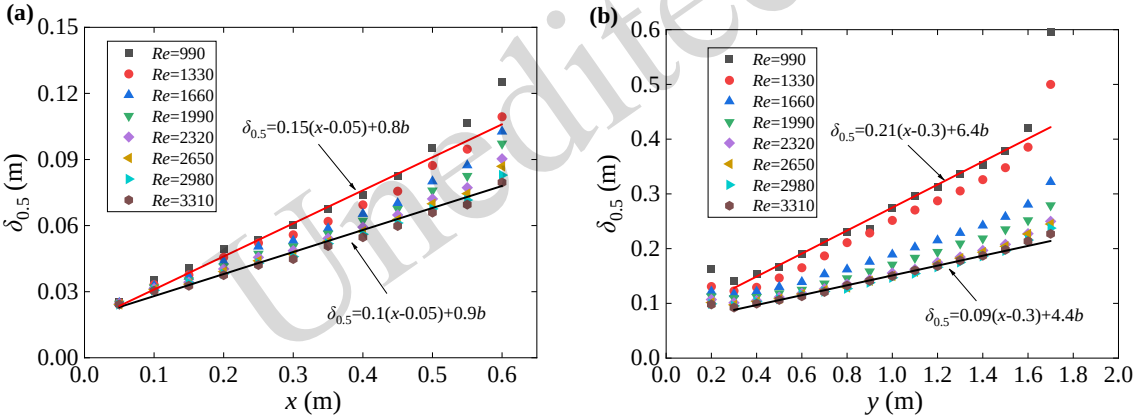

Fig. 13. Characteristic thicknesses of the jet at different Reynolds numbers: (a) attached jet region; (b) free jet region.

Fig. 13 shows that the growth rate of the jet characteristic thickness is related to the *Re* number. The growth rates were about 0.15, 0.14, 0.13, 0.12, 0.11, 0.11, 0.10, 0.10, 0.10 in the attached jet region and 0.21, 0.20, 0.13, 0.11, 0.10, 0.10, 0.09, 0.09 in the free jet region. The growth rate decreases with the increase of *Re* number, and when *Re* ≥ 2650, it is basically independent of the *Re* number. The corresponding functional expressions for the advected jet region and free jet region are described respectively as:

$$\delta_{0.5} = 0.1(x - 0.05) + 0.9b, \tag{11}$$

$$\delta_{0.5} = 0.09(y - 0.3) + 4.4b, \tag{12}$$

4.2.4 Entrainment flow volume of the section

The jet entrainment flow volume can be calculated by integrating the section as:

$$Q_a = \int_0^{\infty} u \mathrm{d}_x, \tag{13}$$

When *Re* ≥ 2650, for attached jets, bringing in the section velocity distribution Eq. (9) yields:

$$\begin{aligned} Q_a &= u_m \delta_{0.5} \int_0^{\infty} 1.48\eta^{1/7}[1 - \mathrm{erf}(0.68\eta)]\mathrm{d}_\eta \\ &= 1.093 u_m \delta_{0.5}, \end{aligned} \tag{14}$$

Bringing in the axial velocity distribution (Eq. (6)) and the jet characteristic thickness (Eq. (11)) yields:

$$Q_a = u_0 \frac{0.109(x + 9b - 0.05)}{0.007(\frac{x}{b})^{1.46} + 1}, \tag{15}$$

The initial flow rate of the jet is:

$$Q_0 = u_0 b, \tag{16}$$

The dimensionless equation is obtained by bringing Eq. (16) into Eq. (15):

Unedited

$$\frac{Q_a}{Q_0}=\frac{0.109(x+9b-0.05)}{b(0.007(\frac{x}{b})^{1.46}+1)}, \quad (17)$$

where Q_a is the entrainment flow volume of any cross section of the attached jet, in m^3/s, and Q_0 is the jet initial air supply flow, in m^3/s.

When $Re \geq 2650$, for a free jet, bringing in the section velocity distribution (Eq. (10)) yields:

$$\begin{aligned} Q_f &= \int_{-\infty}^{\infty} u\mathrm{d}y = 2\int_0^{\infty} u\mathrm{d}y \\ &= 2u_m\delta_{0.5}\int_0^{\infty}[(0.86+\frac{0.14}{1+\eta})\exp(-0.621\eta^2)]\mathrm{d}\eta \\ &= 2.134u_m\delta_{0.5}, \end{aligned} \quad (18)$$

Bringing in the axial velocity distribution (Eq. (7)) and the jet characteristic thickness (Eq. (12)) yields:

$$Q_f = u_0\frac{0.086(y+48.9b-0.3)}{3.37\times10^{-8}(\frac{y}{b})^{3.7}+1}, \quad (19)$$

The dimensionless equation is obtained by bringing Eq. (16) into Eq. (19):

$$\frac{Q_f}{Q_0}=\frac{0.086(y+48.9b-0.3)}{b(3.37\times10^{-8}(\frac{y}{b})^{3.7}+1)}, \quad (20)$$

where Q_f is the entrainment flow volume of any cross section of the free jet, in m^3/s.

5 Discussion

This research has achieved notable advancements in elucidating the flow field characteristics of high-speed train carriages operating under VAV systems. However, several limitations and shortcomings are acknowledged (detailed in Section S4 of the supplementary file).

6 Conclusions

Variable air volume systems are usually used in train operation. To be more in line with the actual operating conditions, the flow field characteristics in train compartments under a variable air volume system were investigated based on isothermal conditions. Subsequently, the relevant equations for the interaction between the variable airflow and the flow field parameters in the train carriage were revealed by combining Prandtl turbulence hypothesis and some classical theories. The main conclusions drawn are as follows:

(1) Influenced by the Coanda effect, the jet enters the compartment and attaches to the ceiling, which is consistent with the characteristics of an attached jet. The two sides of the jet converge and then spread downward, in a manner consistent with the characteristics of a free jet. However, the jet state cannot be fully developed due to the tiny environment of the compartment. Two vortices are formed in the compartment by the jet's entrainment effect.

(2) The isothermal jet development trajectories, velocity profiles, and in-vehicle flow field characteristics all exhibit significant *Re* correlations. A dimensionless treatment of the characteristic parameters of the flow field revealed that the flow characteristics are progressively independent of *Re* when $Re \geq 2650$. Flow field characterization parameters and ventilation parameters can be predicted by combining data and classical theory with fitting.

(3) When $Re \geq 2650$, the axial velocity conforms to the classical $u_m/u_0 \sim (x/b)^r$ or $u_m/u_0 \sim (y/b)^r$ law; the section velocity conforms to the exponential and Gaussian distributions in classical theory; and the jet characteristic thicknesses all conform to a linear distribution.

(4) Through derivation, we found that the jet's entrainment capacity is related to the initial flow rate and the width of the air opening. Improvement of the jet's entrainment capacity is conducive to the improvement of the ventilation efficiency of the system.

In conclusion, this study contributes to a comprehensive explanation and prediction of flow field characteristics under variable air volume systems. It can also provide fast post-prediction data feedback for real-time regulation of variable air volume systems, which has potential for improving thermal comfort and energy saving. Therefore, it is of great significance for the design of air conditioning and ventilation in the railroad industry.

Acknowledgments

This work is supported by National Natural Science Foundation of China (12372049), Fundamental Research Funds for the Central Universities (2682023ZTPY036) and Independent Project of State Key Laboratory of Rail Transit Vehicle System (2023TPL-T06).

Author contributions

Songbo Wu: Investigation, writing-original draft, methodology. **Tian Li:** Conceptualization, funding acquisition,

Unedited

writing-review & editing. **Jiye Zhang:** Resources, funding acquisition.

Conflict of interest

Songbo Wu, Tian Li, and Jiye Zhang declare that they have no conflict of interest.

Data availability

No data were used for the research described in the article.

References

Aliahmadipour M, Abdolzadeh M, Lari K, 2017. Air flow simulation of HVAC system in compartment of a passenger coach. *Applied Thermal Engineering*, 123: 973-990.

Bai JB, Wang SW, Zhang XS, 2008. Development of an adaptive Smith predictor-based self-tuning PI controller for an HVAC system in a test room. *Energy and Buildings*, 40: 2244-2252.

Cao GY, Ruponen M, Kurnitski J, 2010. Experimental investigation of the velocity distribution of the attached plane jet after impingement with the corner in a high room. *Energy and Buildings*, 42: 935-944.

Cao Q, Liu MX, Li XY, et al., 2022. Influencing factors in the simulation of airflow and particle transportation in aircraft cabins by CFD. *Building and Environment*, 207: 108413.

Cao XD, Liu JJ, Pei JJ, et al., 2014. 2D-PIV measurement of aircraft cabin air distribution with a high spatial resolution. *Building and Environment*, 829: 9-1.

Chang ZY, Yi K, Liu WW, 2021. A new ventilation mode of air conditioning in subway vehicles and its air distribution performance. *Energy and Built Environment*, 2(1): 94-104.

Chen CJ, Zheng Q, Yang L, 2024. Adaptive iterative learning control of internal temperature for high-speed trains. *Journal of Mechanical Science and Technology*, 38(1): 463-473.

Glauert M, 1956. The wall jet. *Journal of Fluid Mechanics*. 1(6), 625-643.

Han O, Li AG, 2021. Velocity distribution of wall-attached jets in slotted-inlet ventilated rooms. *Building and Environment*, 194: 107708.

Li AG, 2020. Attachment ventilation theory and design. *China Architecture and Building Press*, Beijing, China, (in Chinese).

Li N, Yang L, Li XD, et al., 2019. Multi-objective optimization for designing of high-speed train cabin ventilation system using particle swarm optimization and multi-fidelity Kriging. *Building and Environment*, 155: 161-174.

Li T, Wu SB, Yi C, et al., 2022. Diffusion characteristics and risk assessment of respiratory pollutants in high-speed train carriages. *Journal of Wind Engineering and Industrial Aerodynamics*, 222: 104930.

Liu, N, Wu, X, Deng, E. et al., 2023. Dust diffusion laws during partition excavation by boom-type roadheader in a metro tunnel. *Tunnelling and Underground Space Technology*, 141: 105382.

Liu PQ, 2008. The theory of free turbulent jets. *Beihang University Press*, Beijing, China, (in Chinese).

Liu WW, Deng QH, Huang WJ, et al., 2011. Variation in cooling load of a moving air-conditioned train compartment under the effects of ambient conditions and body thermal storage. *Applied Thermal Engineering*, 31: 1150-1162.

Liu YK, Yang WC, Deng E, et al., 2024. Using three turbulence simulation methods for modeling the flying of high-speed railway tunnel lining blocks under piston airflow. *Advances in Wind Engineering*, 1(2): 100010.

Lu YB, Wang TT, Zhao CL, et al., 2023. An efficient design method of indoor ventilation parameters for high-speed trains using improved proper orthogonal decomposition reconstruction. *Journal of Building Engineering*, 71: 106600.

Schmeling D, Kuehn M, Schiepel D, et al., 2022. Analysis of aerosol spreading in a German Inter City Express (ICE) train carriage. *Building and Environment*, 222: 109363.

Schmeling D, Volkmann A, 2020. On the experimental investigation of novel low-momentum ventilation concepts for cooling operation in a train compartment. *Building and Environment*, 182: 107116.

Schwarz W, Cosart W, 1961. The two-dimensional turbulent wall-jet. *Journal of Fluid Mechanics*, 10(4): 481-495.

Suresh PR, Srinivasan K, Sundararajan T, et al., 2008. Reynolds number dependence of plane jet development in the transitional regime. *Physics of Fluids*, 205: 04410.

Tian HQ, 2019. Review of research on high-speed railway aerodynamics in China. *Transportation Safety and Environment*, 1(1): 1-21.

Triboix A, Marchal D, 2002. Stability analysis of the mechanism of jet attachment to walls. *International Journal of Heat and Mass Transfer*, 45: 2769-2775.

Verhoff A, 1963. The two-dimensional, turbulent wall jet with and without an external free stream. Princeton Univ NJ.

Wang J, Deng E, Ni YQ, et al., 2024a. Mitigating inflow acceleration effects in twin mountains using air jets: Emphasis on anti-wind for high-speed railways. *Physics of Fluids*, 36(5): 055128.

Wang TT, Zhao KH, Lu YB, et al., 2024b. The airflow characteristics and thermal comfort evaluation in high-speed train cabin with mixing ventilation: An experimental and numerical study. *Building and Environment*, 250: 111187.

Wang TT, Zheng YX, Lu YB, et al., 2024c. Reducing the contaminant dispersion and infection risks in the train cabins by adjusting the inlet turbulence intensity: A study based on turbulence simulation. *Science of the Total Environment*, 930: 172735.

Wang HL, Bi HQ, Zhou YL, et al., 2020. Field measurements and numerical analysis of the energy consumption of urban rail vehicle air-conditioning systems. *Applied Thermal Engineering*, 177: 115497.

Unedited

Woodward H, de Kreij RJB, Kruger ES, et al., 2022. An evaluation of the risk of airborne transmission of COVID-19 on an inter-city train carriage. *Indoor Air*, 32(10): e13121.

Wu F, Dong H, Yu C, et al., 2024. Numerical simulation of formaldehyde distribution characteristics in the high-speed train cabin. *Building Simulation*, 17: 285-300.

Wu SB, Li T, Zhang JY, 2023. Effect of combined side-wall air supply on ventilation and respiratory pollutant dispersion characteristics of high-speed trains. *Engineering Applications of Computational Fluid Mechanics*, 17(1): 2272646.

Xu RZ, Wu F, Li XL, et al., 2022. Numerical comparison of ventilation modes on the transmission of coughing droplets in a train compartment. *Journal of Wind Engineering and Industrial Aerodynamics*, 231: 105240.

Yang WC, Wang J, Deng E, et al., 2024. A hybrid ventilation scheme applied to bidirectional excavation tunnel construction with a long inclined shaft. *Journal of Central South University*, 31: 3187-3205.

Yang L, Li MX, Li XD, et al., 2018. The effects of diffuser type on thermal flow and contaminant transport in high-speed train (HST) cabins - a numerical study. *International Journal of Ventilation*, 17(1): 48-62.

Yin HG, Huo YK, Wang YY, et al., 2021. Numerical investigation on mechanisms and performance of column attachment ventilation for winter heating. *Building and Environment*, 202: 108025.

Yu H, Liao CM, Liang HM, 2003. Scale model study of airflow performance in a ceiling slot-ventilated enclosure: isothermal condition. *Building and Environment*, 38(11): 1271-1279.

Zhang JL, Li XM, Zhao TY, et al., 2015. Experimental study on a novel fuzzy control method for static pressure reset based on the maximum damper position feedback. *Energy and Buildings*, 108: 215-222.

Electronic supplementary materials

Sections S1–S4, Table S1, Figs. S1–S3, equations S1–S5

中文概要

题　目：基于变风量系统射流通风的列车车厢内流场特性研究：等温条件

作　者：吴松波，李田，张继业

机　构：西南交通大学，轨道交通运载系统全国重点实验室，中国成都，610031

目　的：变风量系统在列车中得到了广泛应用，因为它们能为空调提供有效的节能效果。然而，设计阶段通常是在一定的固定气流下进行的，这导致了预期流场与实际流场之间的差异。本文旨在分析基于等温条件的变风量系统下的车内流场特性，进而建立了风量与流场参数间的关联方程。

创新点：1. 通过数值模拟方法，探究了变风量与列车车厢内流场特性之间的关系；2. 基于射流力学理论，建立了通风参数与射流之间的参数关联式。

方　法：1. 通过数值模拟方法，明晰了风量变化与列车车厢内速度分布、涡量分布以及流线分布特征之间的关系（图 4–图 9）；2. 基于贴附射流和自由射流的流动理论，构建了等温工况下列车车厢内的通风参数关联式（公式(5)–公式(12)）；3. 通过理论推导，得出断面卷吸流量与流量和风口宽度之间的关系（公式(13)–公式(20)）。

结　论：1. 刚进入车厢的气流符合附壁射流特性，中间汇合后则符合自由射流特性；2. 流场特性与雷诺数（*Re*）显著相关，且受车内有限空间限制；3. 当 *Re* ≥ 2650 时，轴向速度符合经典 u_m/u_0~$(x/b)^r$ 或 u_m/u_0~$(y/b)^r$ 规律，断面速度呈指数和高斯分布，射流特征厚度呈线性分布；4. 推导显示，卷吸流量主要与初始流量和出风口宽度有关。

关键词：高速列车；内部流场；通风；CFD 模拟

Unedited